

Full length article

Micromechanical behavior and thermal stability of a dual-phase $\alpha+\alpha'$ titanium alloy produced by additive manufacturing

Charlotte de Formanoir^{a,b,*}, Guilhem Martin^c, Frédéric Prima^d, Sébastien Allain^{e,f}, Thibaut Dessolier^c, Fan Sun^d, Solange Vivès^a, Benjamin Hary^a, Yves Bréchet^c, Stéphane Godel^a

^a 4MAT, Université Libre de Bruxelles, 50 Av. F.D. Roosevelt (CP 165/63), 1050, Bruxelles, Belgium

^b KU Leuven, Dept. of Mechanical Engineering, Celestijnenlaan 300, Heverlee, Belgium

^c Univ. Grenoble Alpes, CNRS, Grenoble INP, SIMaP, F-38000, Grenoble, France

^d PSL Research University, Chimie ParisTech, CNRS, Institut de Recherche de Chimie Paris, 75005, Paris, France

^e Institut Jean Lamour, UMR 7198 CNRS - Université de Lorraine, Campus ARTEM, 54000, Nancy, France

^f Laboratory of Excellence on Design of Alloy Metals for Low-mAss Structures (Labex DAMAS), Université de Lorraine, France

ARTICLE INFO

Article history:

Received 3 April 2018

Received in revised form 19 September 2018

Accepted 23 September 2018

Available online xxx

Keywords:

Ti—6Al—4V

Heat treatment

Martensite

Work-hardening

Additive manufacturing

ABSTRACT

In order to improve the tensile properties of additively manufactured Ti—6Al—4V parts, specific heat treatments have been developed. Previous work demonstrated that a sub-transus thermal treatment at 920 °C followed by water quenching generates a dual-phase $\alpha+\alpha'$ microstructure with a high work-hardening capacity inducing a desirable increase in both strength and ductility. The present study investigates the micromechanical behavior of this $\alpha+\alpha'$ material as well as the thermal stability of the metastable α' martensite. To that end, annealing of the $\alpha+\alpha'$ microstructure is performed and the resulting microstructural evolution is analyzed, along with its impact on the tensile properties. A deeper understanding of the micromechanics of the multi-phase microstructure both before and after annealing is achieved by performing in-situ tensile testing within a SEM, together with digital image correlation for full-field local strain measurements. This approach allows the strain partitioning to be quantified at a microscale and highlights a significant mechanical contrast between the two phases. In the $\alpha+\alpha'$ microstructure, the α' phase is softer than the α phase, which is confirmed by nanoindentation measurements. Partial decomposition of the martensite during annealing induces a substantial hardening of the α' phase, which is attributed to fine-scale precipitation and solution strengthening. A scale transition model based on the iso-work assumption and describing the macroscopic tensile behavior of the material depending on the individual mechanical behavior of each phase is also proposed. This model enables to provide insights into the underlying deformation and work-hardening mechanisms.

© 2018.

1. Introduction

Due to their high strength-to-density ratio and corrosion resistance, titanium alloys, and Ti—6Al—4V in particular, are widely used in structural aerospace applications, where the payoff for weight reduction is high [1]. A relatively low Young's modulus and excellent biocompatibility also make Ti—6Al—4V a choice material for biomedical devices [2]. However, its comparatively low ductility and lack of work-hardening, with consequences on toughness performances, still limit its use in many applications when compared to other metals such as steels [3]. Moreover, because of their high strength, low thermal conductivity, chemical reactivity with tool materials, and 'catastrophic shear' chips formation, machining of titanium components often remains a challenge [4]. This is a critical is-

sue in terms of cost and productivity, especially when complex geometries are required. In particular, very high "buy-to-fly" ratios (up to 40:1) can be reached when machining aerospace components, further increasing their cost [5].

The recent developments of additive manufacturing (AM) offer new design opportunities and the possibility to produce light-weight structures with a "buy-to-fly" ratio close to 1:1 [5]. However, several challenges have yet to be overcome if one aims at considering powder-bed AM processes such as Selective Laser Melting (SLM) and Electron Beam Melting (EBM) as proper industrial tools. Those challenges include poor surface finishing [6–8], porosity [9,10] and residual stresses [11]. In order to tackle these issues, post-treatments are usually applied to the near-net shape parts, such as machining or chemical etching to improve the surface finish [8,12–14], Hot Isostatic Pressing (HIP) to increase the relative density [6,9,10,15] and improve the fatigue properties, or stress-relief [16]. The fully martensitic microstructure and high residual stresses observed in as-built SLM parts are very detrimental in terms of ductility [17,18]. Hence, the classical thermal pathway for post-processing of Ti—6Al—4V

* Corresponding author. 4MAT, Université Libre de Bruxelles, 50 Av. F.D. Roosevelt (CP 165/63), 1050, Bruxelles, Belgium.

Email address: charlotte.deformanoir@kuleuven.be (C. de Formanoir)

SLM specimens includes a stress relief at 650 °C for several hours [19], which induces a complete decomposition of the martensite [18,20,21]. For both EBM and SLM parts, the presence of lack-of-fusion residual porosities can be addressed by HIP at 920 °C, which results in a coarsening of the α lamellae and the β rods [15,22,23]. Stress relief and HIP have demonstrated their efficiency in increasing the ductility of AM parts [15,21,23]. However, they only enable a very limited control over the microstructure, which remains far from being optimized after post-processing. The resulting lamellar $\alpha+\beta$ microstructure still exhibits a lower ductility than what is typically observed in a wrought material. In comparison, during the processing of wrought Ti—6Al—4V, equiaxed or bimodal microstructures that exhibit more balanced mechanical properties are obtained by hot deformation [24]. Such thermo-mechanical treatments cannot be performed on AM parts since they already have a near-net shape in their as-built condition. In terms of microstructural optimization, this is a major limitation. In order to further improve the mechanical properties of AM parts, in particular their ductility and strain-hardening capacity, microstructure engineering through innovative heat treatments should therefore be considered.

Fully martensitic Ti—6Al—4V exhibits poor mechanical properties [17,18], so that martensite is systematically avoided or intentionally decomposed. However, the detrimental impact of martensite is no longer observed when the microstructure consists in a mixture of both martensite and α phase. De Formanoir et al. recently reported that a very broad range of tensile properties can be obtained when performing *sub-transus* treatments followed by *water quenching*, generating a dual-phase $\alpha+\alpha'$ microstructure in Ti—6Al—4V parts produced by EBM. Depending on the annealing temperature in the $\alpha+\beta$ range, the phase proportion can be varied. This comes with a change in the composition of each phase since the β phase – which in turn transforms into α' upon quenching – gets enriched in vanadium as the annealing temperature decreases. By finely adjusting the α/α' phase proportions, a remarkable improvement of the tensile behavior can be achieved. It was found that a simultaneous increase in ultimate tensile strength and elongation at fracture was observed when annealing was performed at a temperature of about 920 °C, resulting in a α phase fraction of about 50% [25].

The present paper aims at investigating the origin of the unusual work-hardening behavior observed in this optimized dual-phase $\alpha+\alpha'$ microstructure. α' martensite being an out-of-equilibrium phase, its thermal stability has to be assessed. This topic is addressed by studying the microstructural evolution of dual-phase $\alpha+\alpha'$ Ti—6Al—4V for different annealing temperatures and annealing times and the resulting impact on the material's tensile properties. In order to have a deeper understanding of the micromechanics of the multi-phase microstructure, the deformation of each individual phase is measured at the grain scale by performing in-situ tensile testing within a Scanning Electron Microscope (SEM), together with digital image correlation (DIC). A homogenization model based on the iso-work assumption and describing the macroscopic tensile behavior of the material, depending on the individual mechanical behavior of each phase, is also developed. This model enables to shed light on the origin of the enhanced work hardening capacity of the dual phase $\alpha+\alpha'$ microstructures and the change of mechanical behavior associated to the thermal decomposition of martensite.

2. Materials and methods

All specimens were manufactured by EBM, using an Arcam AB[®] A2 machine, with the standard ARCAM melting parameters and a layer thickness of 70 μm . For more information about these parameters, the reader is referred to de Formanoir et al. [26]. The chemical composition of the Ti—6Al—4V powder used as starting material is reported in Table 1.

The specimens underwent Hot Isostatic Pressing (HIP) – i.e. 2 h at 920 °C under a pressure of 1000 bar followed by slow furnace cooling [6,15]. Several samples were then submitted to a sub-transus heat treatment, performed at a temperature of 920 °C, for 2 h, followed by water quenching, in order to obtain a dual-phase $\alpha+\alpha'$ microstructure with about 50% of α phase [25]. To investigate the effect of martensite decomposition, a further annealing of 1 h at 500 °C, 5 min at 700 °C or 1 h at 700 °C was performed. Throughout this paper, the specimens will be referred to as “920-WQ”, “500-1h”, “700-5min”, “700-1h”, respectively. During all thermal treatments, the samples were encapsulated in quartz tubes filled with argon in order to avoid oxygen contamination.

The resulting microstructures were characterized by SEM, Transmission Electron Microscopy (TEM) (JEOL 2000 EX), and X-Ray Diffraction (XRD) (X'Pert Pro by PANalytical, Cu K α radiation, scan step of 0.017°, counting time of 4 s). Based on the XRD data, the lattice parameters of each phase were determined by Le Bail analysis. Electron Probe Micro Analyzer (EPMA) measurements were performed on the “920-WQ” specimen with a 15 kV accelerating voltage and 15 nA probe current.

For the evaluation of macroscopic tensile properties, tensile specimens were machined from EBM cylindrical specimens built with a sacrificial extra-thickness of 0.5 mm to limit the detrimental effect of the as-built surface roughness [12]. The tensile axis was aligned with the build direction of the specimens. The geometry of the tensile specimens is reported in Fig. 1 a. Tensile testing was carried out at room temperature, to fracture, and the deformation was measured with an extensometer at a cross-head speed of 1 mm/min. The conventional yield strength $\sigma_{y,0.2\%}$ was approximated by measuring the proof stress at 0.2% plastic strain. The reduction of area of each specimen was measured by SEM analysis of the fracture surface.

For micromechanical characterization, flat tensile specimens (Fig. 1b) were extracted from EBM cuboids using electrical discharge machining (EDM). The specimens were mirror-polished with an OPS +10% H₂O₂ solution and the microstructure was revealed by dipping the polished specimens in Kroll's reagent (2% HF, 4% HNO₃ in water) for 20s. In order to measure the deformation of each phase, tensile tests were performed in a ZEISS Gemini SEM500 using a Deben MT2000 EW *in-situ* tensile stage equipped with a homemade Lab-View interface allowing an accurate control of the strain rate. A strain rate of 10⁻³ s⁻¹ was used. For each specimen, successive high-definition images (4121 × 3253 pixels) of the same region of interest were acquired at different strain increments using secondary electron contrast (SE) with an acceleration voltage of 15 kV. High definition imaging (pixel size ~13 nm) was required to achieve a good description of the local contrast combined with a relatively large field of view to ensure the statistical consistency of the local strain mapping. The com-

Table 1
Chemical composition of the ARCAM Ti—6Al—4V powder used in the EBM process.

Element	Al	V	C	Fe	O	N	H	Ti
wt. %	6%	4%	0.03%	0.10%	0.15%	0.01%	0.003%	balance

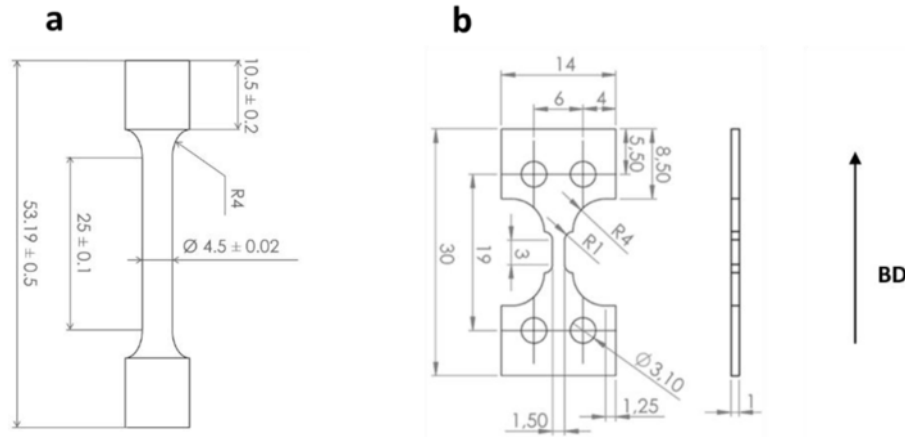


Fig. 1. Schematic showing the geometry and dimensions of (a) the cylindrical specimens used for “macroscopic” tensile testing and (b) the flat specimens used for “in-situ” tensile testing within the SEM. The arrow indicates the building direction in additive manufacturing.

parison between undeformed (Fig. 2a) and deformed (Fig. 2b) states allows a quantitative characterization of the strain distribution to be obtained. It should be highlighted that the deposition of a micro-grid or of a random speckle at the surface of the specimen was not required. Indeed, the microstructure pattern itself, and more specifically the local contrast induced by etching, allowed digital image correlation to be performed, as illustrated in Fig. 2. DIC was performed using CMV software [27,28]. For a more detailed description of the DIC routine applied here, the reader is referred to Martin et al. [29,30] and Lechartier et al. [31] In order to determine the strain partitioning between α and α' -martensite, the strain map had to be related to the underlying microstructure. The SE-images were subdivided

in subsets of 60×60 pixels, i.e. $\sim 800 \times 800 \text{ nm}^2$, and manual segmentation was performed in order to differentiate the α phase from the α' phase, as shown in Fig. 2c. The acicular morphology of the α' martensite allowed a clear and unambiguous identification of this phase to be performed. Etching introduces some relief as shown in Fig. 2a with the α phase standing out from the surface either lower or higher than the α' phase (see yellow arrows in Fig. 2a).

For further characterization of the mechanical behavior of the α and α' phases, nanoindentation was performed on a “920-WQ” specimen with an Anton-Paar Nano-Indenter. A map of 21×21 indents over $50 \times 50 \mu\text{m}^2$ (i.e. a distance between indents of $2.5 \mu\text{m}$) was generated, using a load of 10 mN and a holding time of 10 s .

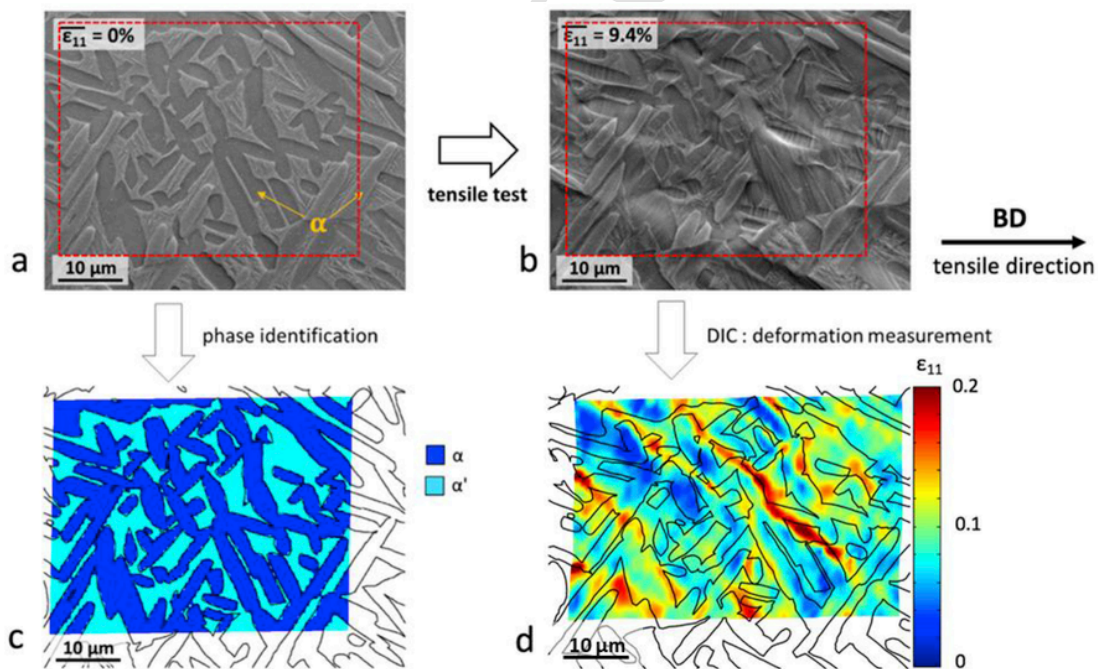


Fig. 2. Experimental procedure to determine the strain partitioning from the images acquired during “in-situ” tensile tests on a “920-WQ” specimen. (a) SEM-SE image of the undeformed microstructure in the region of interest. (b) SEM-SE image of the deformed microstructure in the region of interest. (c) Phase identification to distinguish subsets within the α phase (dark blue) from those located within the α' -martensite (light blue), interphase boundaries are highlighted in black. (d) Example of a strain map obtained from DIC measurements representing the deformation along the tensile direction, ϵ_{11} . (For interpretation of the references to color in this figure legend, the reader is referred to the Web version of this article.)

Both in-situ tensile testing coupled with DIC and nanoindentation were also performed on a “500-1h” specimen, in order to evaluate the effect of martensite decomposition on the micromechanical behavior of the material.

3. Results

3.1. Microstructure analysis

3.1.1. SEM imaging

As illustrated in Fig. 3 a, as-HIP'ed parts exhibit a typical $\alpha+\beta$ microstructure. 3–4 μm thick α lamellae are delineated by a residual β matrix made of thin β rods. HIP results in a coarsening of the α lamellae compared to an as-built microstructure. However, this sub-transus treatment does not induce any change in the size or in the tex-

ture of the parent β grains, which were thus consistent for all specimens. Sub-transus heat treatments performed at 920 °C lead to a dual-phase $\alpha+\alpha'$ microstructure, as previously reported by de Formanoir et al. [25]. As can be observed in Fig. 3 b, coarse α lamellae coexist with much thinner acicular α' laths, which are about 100–200 nm thick. These thin laths result from the martensitic transformation of the high temperature β phase on quenching. EPMA measurements performed on a “920-WQ” specimen demonstrate a significant partitioning of both V and Al, with 2.27 ± 0.13 wt% V and 6.56 ± 0.12 wt% Al in α , whereas the α' phase contains 5.89 ± 0.21 wt% V and 5.08 ± 0.05 wt% Al.

After a further 1 h annealing step at 500 °C, the microstructure remains very similar to that of as-quenched specimens, see Fig. 3 c. However, at a higher temperature, namely 700 °C, a clear evolution of the microstructure can be observed. After 5 min (Fig. 3d) the typical

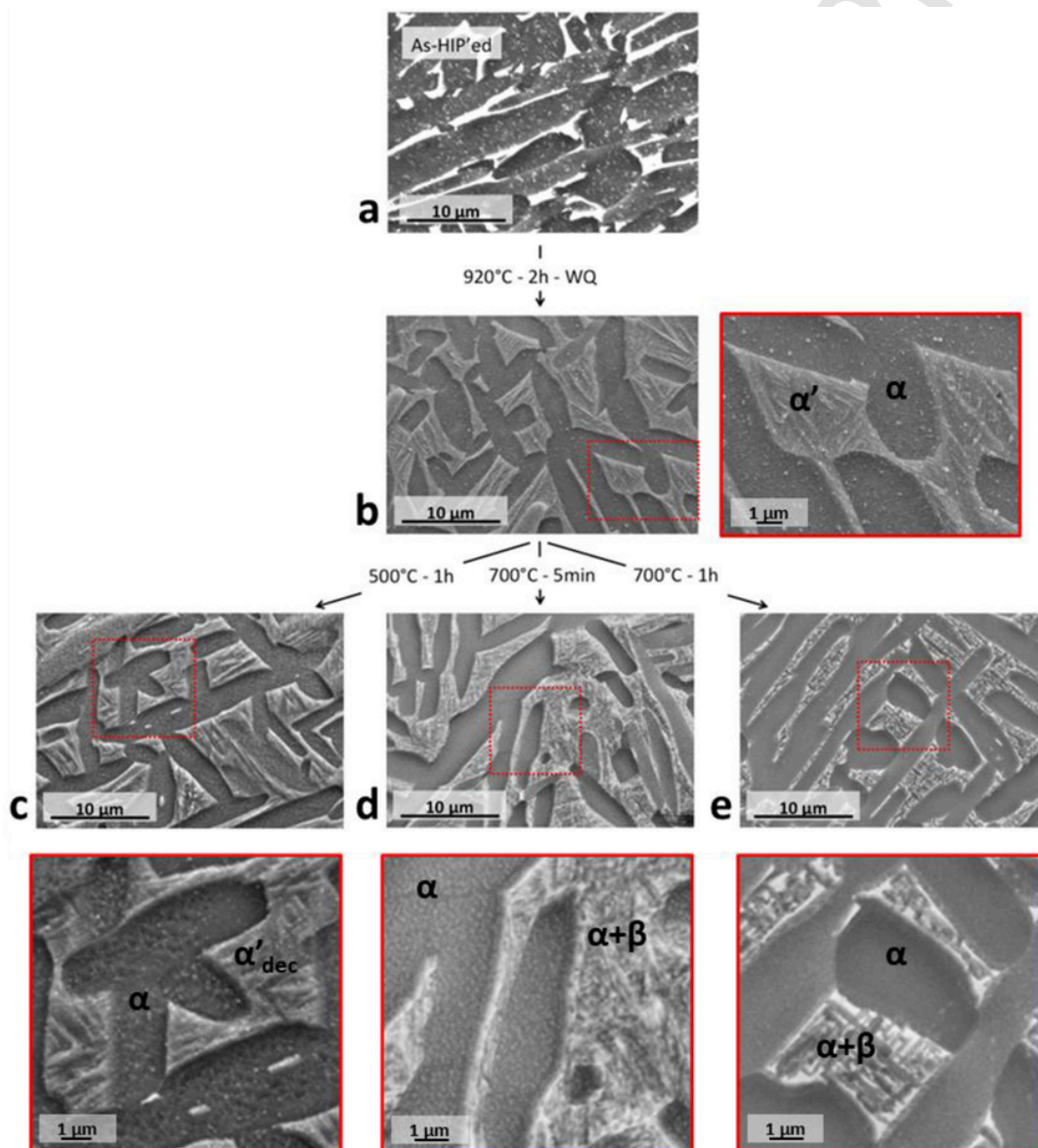


Fig. 3. SEM micrographs of as-HIP'ed and heat-treated specimens (BSE contrast after etching): (a) as-HIP'ed: α lamellae and β rods; (b) HIP + 920 °C, 2 h, water quenched: α lamellae and fine needles of α' martensite; (c) HIP + 920 °C, 2 h, water quenched + 500 °C, 1 h, air cooled: α lamellae and fine needles of partially decomposed α'_{dec} ; (d) HIP + 920 °C, 2 h, water quenched + 700 °C, 5 min, air cooled: α lamellae and fine $\alpha+\beta$; (e) HIP + 920 °C, 2 h, water quenched + 700 °C, 1 h, air cooled: α lamellae and fine $\alpha+\beta$.

acicular morphology of the α' martensite is no longer observed. After a longer annealing time of 1 h (Fig. 3e), the previously martensitic areas exhibit a fine $\alpha+\beta$ morphology. A bimodal microstructure is thus obtained. It consists of a mixture of relatively coarse primary α laths and much thinner (about 200 nm thick) secondary α lamellae delineated by β phase, resulting from the complete decomposition of the α' martensite.

3.1.2. X-ray diffraction

In order to confirm the nature of the phases present in the material, X-ray diffraction (XRD) was performed on all five specimens

(Fig. 4a). As previously reported by de Formanoir et al. [25], the “920-WQ” specimen, which contains 50% of α phase and 50% of α' martensite, is characterized by a splitting of the $(0002)_\alpha$ and $(10-12)_\alpha$ peaks (see arrows in Fig. 4a), which gives evidence of the presence of α' martensite. After annealing at 500 °C, a relatively broad $(10-12)_\alpha$ peak can still be observed, but to a lower extent than in the “920-WQ” specimen. This is even more the case in the specimens annealed at 700 °C. This can be related to a progressive change in chemical composition occurring during martensite decomposition.

All annealed samples display a clear β peak, which is not observed in the reference “920-WQ” specimen. This β peak is broader

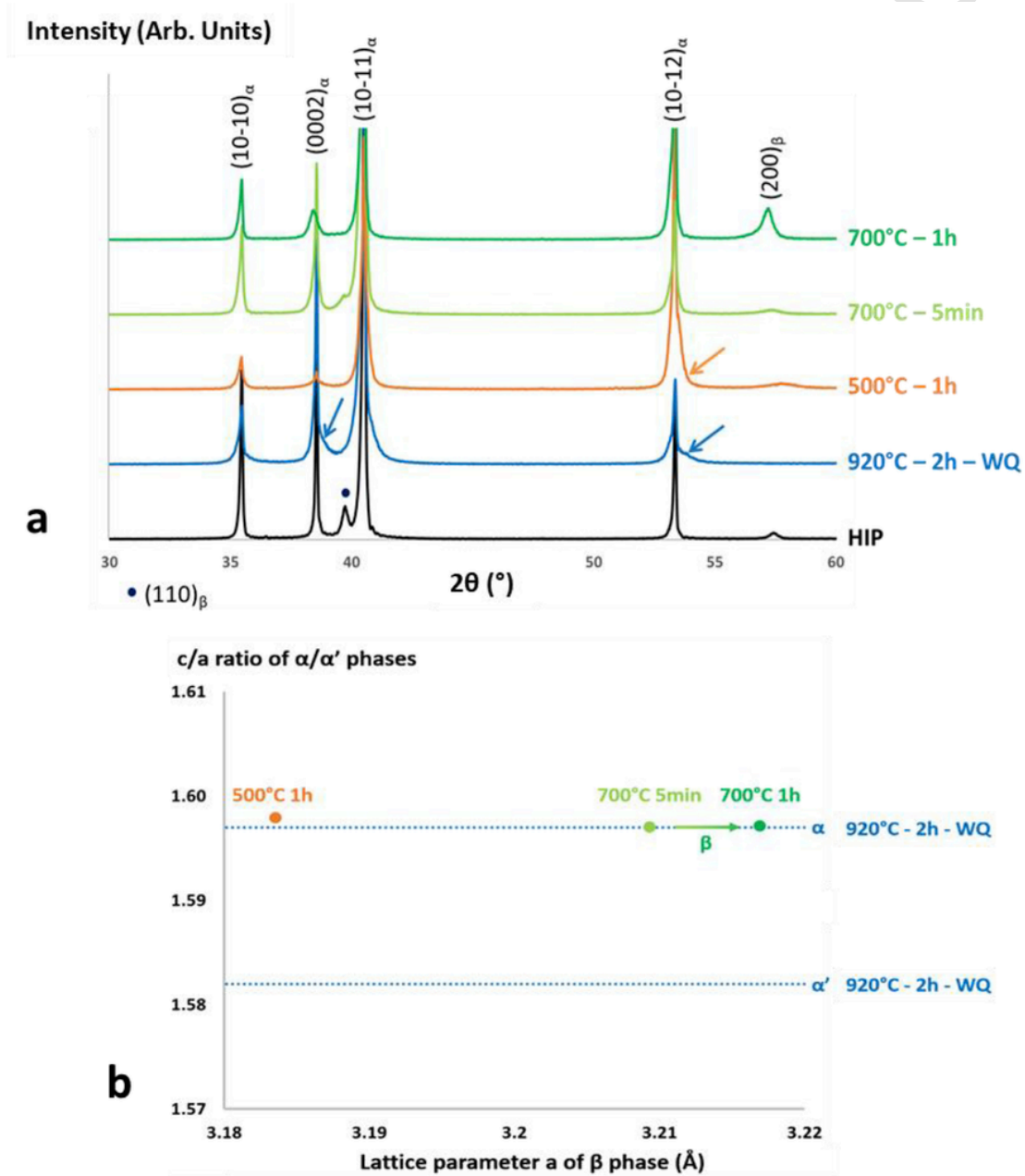


Fig. 4. (a) XRD profiles of the heat-treated specimens. The arrows highlight splitting or broadening of the $(0002)_\alpha$ and $(10-12)_\alpha$ peaks. (b) Lattice parameters deduced from the XRD measurements. The c/a ratio of the decomposing α' phase and the lattice parameter of the β phase are reported for the “500-1h”, “700-5min” and “700-1h” specimens. The dotted blue lines give the c/a ratio of the α and α' phases in the “920-WQ” specimen. (For interpretation of the references to color in this figure legend, the reader is referred to the Web version of this article.)

in the “500-1h” specimen than in the specimens annealed at 700 °C, indicating a coarsening of the β grains as the annealing temperature increases.

Based on the XRD data, the lattice parameters of the α , α' and β phases were determined by Le Bail analysis. Fig. 4 b shows a significant increase of the a lattice parameter of the β phase during decomposition: it varies from 3.18 Å at 500 °C to 3.22 Å at 700 °C.

3.1.3. TEM analysis

TEM analysis was performed on a “920-WQ” specimens and is reported in Fig. 5. The fine acicular needles of α' martensite are here clearly visible. TEM analysis of the “500-1h” microstructure, shown in Fig. 6, demonstrated the presence of β phase in the previously martensitic areas. Very fine α lamellae, which are about 100–200 nm thick, are surrounded by a dispersion of equally fine β (Fig. 6 e and Fig. 6f). Several α variants can be observed, two of which are shown in Fig. 6 c and Fig. 6 d. For the β phase, on the other hand, only one orientation is observed.

3.2. Mechanical properties

3.2.1. Tensile properties

The tensile curves of as-HIP'ed and heat-treated parts are reported in Fig. 7. The engineering stress-strain curves until fracture and the true stress-strain curves until necking are shown in Fig. 7 a and Fig. 7 b, respectively. As reported in Table 2, the “920-WQ” tensile specimens exhibit a 100 MPa increase in ultimate tensile strength (UTS) along with an increase in both uniform strain and reduction of area compared to as-HIP'ed specimens. However, this occurs at the expense of the yield strength $\sigma_{y,0.2\%}$, which is lowered by about 100 MPa. A remarkable work-hardening is observed for the dual-phase $\alpha+\alpha'$ microstructure. $\Delta\sigma$, defined as the difference between true UTS σ_m and yield strength $\sigma_{y,0.2\%}$ reaches 353 ± 44 MPa in these specimens, whereas it is of only 142 ± 56 MPa in the as-HIP'ed conditions. This behavior is better reflected in Fig. 7 c, which reports the work-hardening coefficient n_{incr} as a function of strain: $n_{incr} = \frac{d \ln(\sigma)}{d \ln(\epsilon)}$, using an approach first proposed by Sachdev [32]. Throughout the entire deformation range, n_{incr} remains substantially higher for the “920-WQ” specimens than for the “as-HIP'ed” specimens, so that

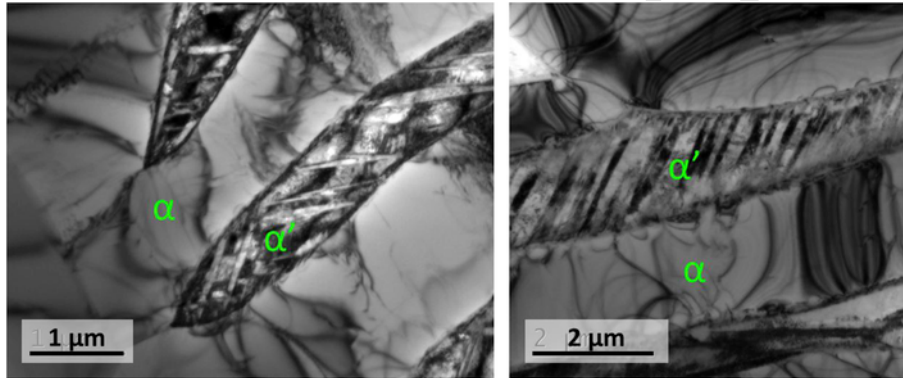


Fig. 5. TEM micrographs of a “920-WQ” specimen.

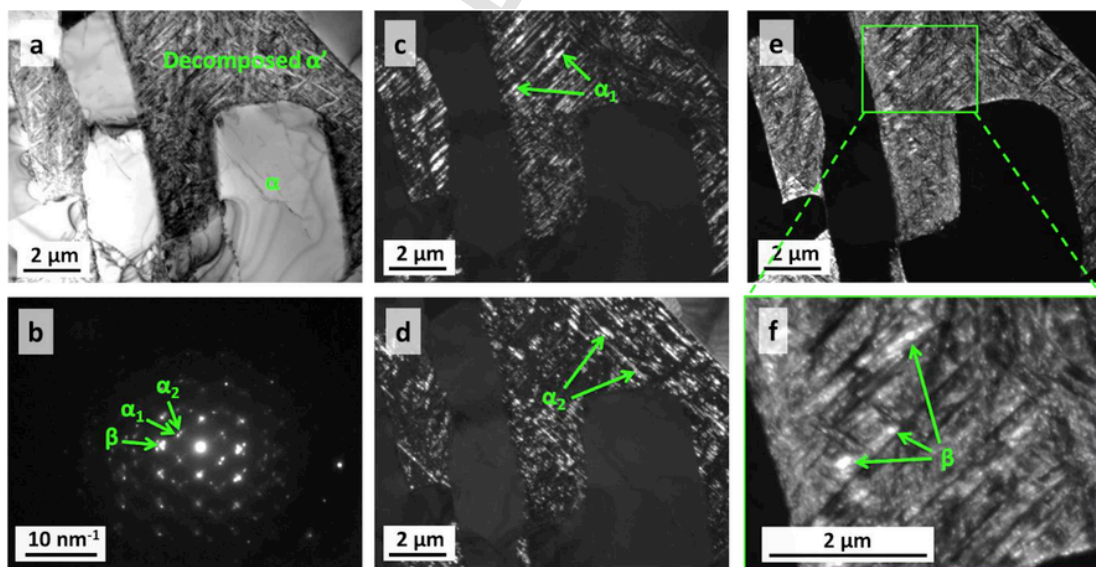


Fig. 6. TEM analysis of a “500-1h” specimen. Bright field (a), diffraction pattern (b), and dark field images of each α variant (c, d) and of the β phase (e, f).

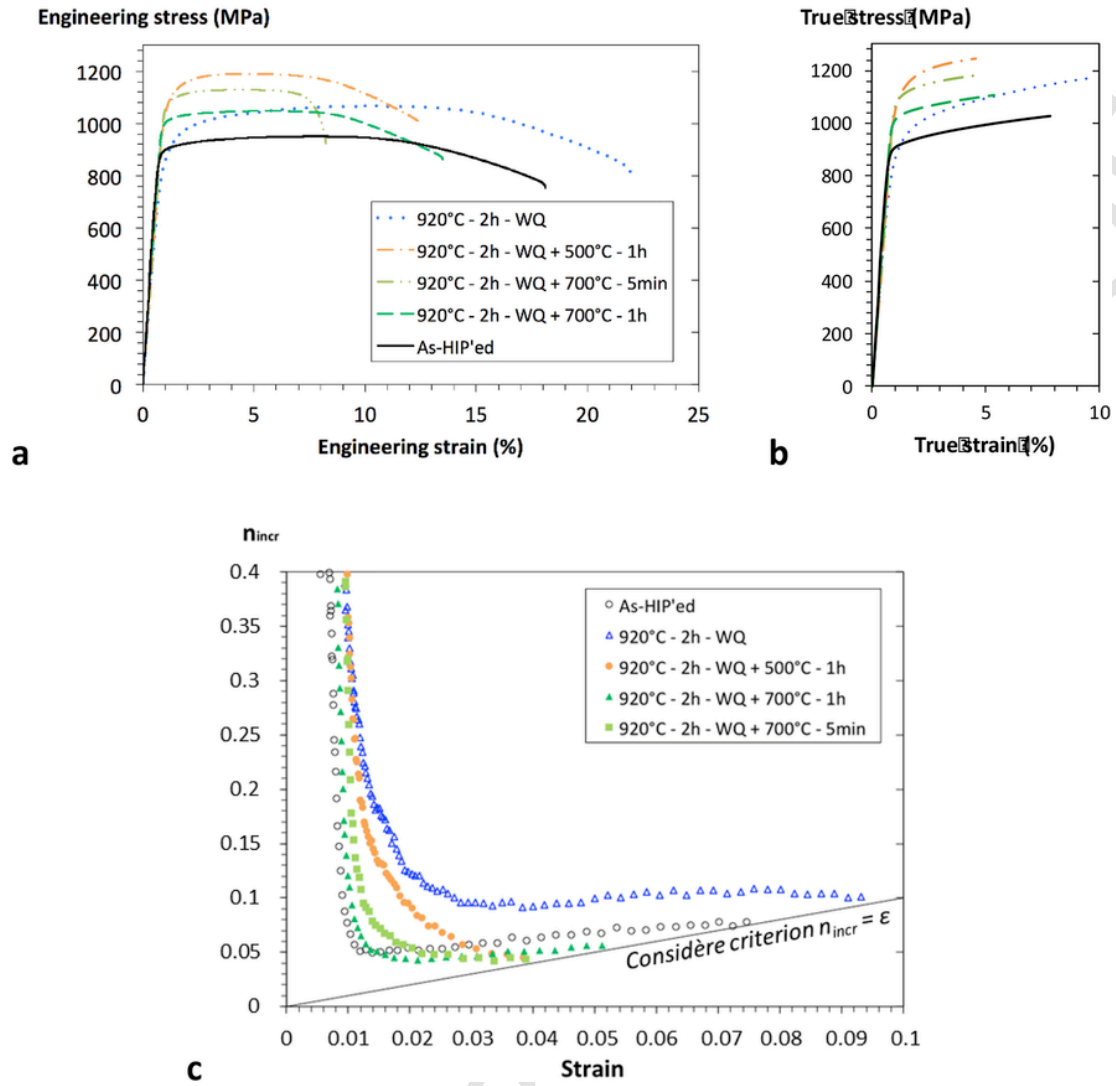


Fig. 7. (a) Engineering and (b) true stress-strain curves of heat-treated tensile specimens. Two or three specimens were tested in each condition to ensure the reproducibility of the results but only one typical stress-strain curve is shown. (c) Work-hardening coefficient as a function of strain. Considère's criterion for the onset of necking is also drawn.

Table 2

Heat treatment and resulting yield strength σ_y , engineering ultimate tensile strength (UTS) R_m , true UTS σ_m , true uniform strain ϵ_u , $\Delta\sigma = \sigma_m - \sigma_{y,0.2\%}$, and reduction of area A_r .

	$\sigma_{y,0.2\%}$ (MPa)	R_m (MPa)	σ_m (MPa)	$\Delta\sigma$ (MPa)	ϵ_u (%)	A_r (%)
As—HIP'ed	914±20	971±22	1056±34	142±56	8.6±2.1	38±11
920°C - 2 h - WQ	825±33	1073±7	1186±11	353±44	11±0.3	41±11
+500 °C - 1 h	1088±9	1194±4	1247±1	159±8	4.3±0.3	25±6
+700 °C - 5 min	1083±5	1123±10	1182±2	98±7	4.5±0.1	33±12
+700 °C - 1 h	1012±6	1047±1	1113±8	101±14	6.1±0.8	38±7

Considère's criterion for the onset of necking $n_{incr} = \epsilon$ occurs at a substantially higher strain value for the “920-WQ” specimens.

The “500-1h” specimens exhibit a considerable increase in yield strength ($\sigma_{y,0.2\%} = 1088 \pm 9$ MPa) and, to a lower extent, in UTS ($\sigma_m = 1247 \pm 1$ MPa) compared to the “920-WQ” specimens ($\sigma_{y,0.2\%} = 825 \pm 33$ MPa, $\sigma_m = 1186 \pm 11$ MPa). However, this high strength comes along with lower uniform elongation and reduction of area. At 700 °C, for an annealing time of 5 min, this important increase in yield strength is also observed ($\sigma_{y,0.2\%} = 1083 \pm 5$ MPa). However, the UTS does not follow the same trend, as it remains in the same range as that

of the “920-WQ” specimens. A longer annealing time of 1 h at 700 °C leads to a further decrease in both yield strength and UTS and an increase in ductility with a reduction of area similar to the one obtained in the “as-HIP'ed” conditions.

As highlighted in Fig. 7 c when the annealing time and temperature increase, the work hardening coefficient tends to decrease at low strains. In the “500-1h” specimens, a steep decrease in work hardening is observed until necking occurs at a true strain of $4.3 \pm 0.3\%$. For the “700-5min” and “700-1h” specimens, the work-hardening coefficient, although initially lower than that of the “500-1h” specimens,

eventually reaches a plateau at $n_{\text{incr}} \sim 0.05$, so that necking occurs at higher strains. In other words, as the annealing temperature and time increase, the work-hardening behavior approaches that of the as-HIP'ed specimen, although the stress levels are different.

3.2.2. Nanoindentation

The nanoindentation measurements were performed as a regular grid on a “920-WQ” and on a “500-1h” specimen, see Fig. 8 a and Fig. 8 d, respectively. In the “920-WQ” material, the nano-hardness distributions within the α' -martensite and the α -phase are displayed in Fig. 8 b and Fig. 8 c, respectively. It turns out that the α' -martensite is the softer phase with an average of 4.97 ± 0.3 GPa, while the harder one is the α -phase with an average hardness reaching 6.28 ± 0.65 GPa. After a 1 h-annealing step at 500°C , the α'_{dec} phase – i.e. the partially decomposed martensite – sees its average hardness greatly increased up to 6.09 ± 0.25 GPa (Fig. 8e), whereas the α -phase exhibits a similar hardness of 6.24 ± 0.40 GPa (Fig. 8f). Note that, for both conditions, the nano-hardness distributions reported in Fig. 8b, 8c, 8e and 8 f include all data whereas the calculation of the average nano-hardness was done excluding the indents located in the vicinity of interfaces.

3.2.3. In-situ tensile tests and strain partitioning

In order to get further insights into the mechanical behavior of the multiphase microstructure, full-field strain measurements using DIC were performed from SEM–SE micrographs acquired at different increments of strain during in-situ tensile testing. The approach previously detailed in Fig. 2 allowed the strain within each phase to be quantified. Two different samples, namely a “920-WQ” and a “500-1h”, were tested. It should be highlighted that the martensite, which is a discontinuous arrangement of auto-accommodated α' needles, is considered here as a monolithic phase whose average tensile behavior is compared, at the grain/phase scale, to that of the continuous α phase.

Typical strain maps of the tensile strain ϵ_{11} obtained after different plastic strain increments, for a “920-WQ” specimen and a “500-1h” specimen, are shown in Fig. 9 and Fig. 10, respectively. The strain

ϵ_{11} , i.e. the strain along the tensile direction, is considered. The data are represented as color maps corresponding to different levels of local strain. In both conditions, the ϵ_{11} strain maps show that the deformation is highly heterogeneous with some areas being only slightly deformed while others are more strongly distorted.

It can be observed that in the $\alpha+\alpha'$ “920-WQ” specimens, the largest deformations are mostly located in the martensitic α' phase, see Fig. 9. At low levels of macroscopic deformation, Fig. 9 b strongly suggests that the plastic deformation initiates in martensitic areas. This is further reflected by the strain histogram displayed in Fig. 9 d since the strain distribution functions of the α -phase and the overall strain distribution functions are superimposed for the low strain values. Similarly, at large strain, the distribution function of the α' -martensite is superimposed on that of the overall strain. It means that the most deformed regions are always located in martensite. As the strain increases, the deformation spreads to adjacent areas (Fig. 9c) and the distributions of the two phases tend to converge (Fig. 9e), but the martensite remains more deformed than the α phase. Locally, the deformation of the α' martensite can reach 2 to 3 times that of the adjacent α phase. When computing the average deformation of each phase as a function of the overall macroscopic deformation of the tensile specimen (Fig. 11a), it can be noticed that, from the initiation of plastic deformation in the material to high deformation levels, the α' phase remains the softer phase, being about 30% more deformed than the harder α phase.

Interestingly, in the “500-1h” specimens (Fig. 10), the strain partitioning is inverted, i.e. after an annealing step at 500°C , the α phase becomes the softer phase whereas the former martensitic regions can now be considered as the harder phase. In Fig. 10 c, the local deformation of the α phase is almost systematically higher than that of the adjacent α'_{dec} phase. This is better illustrated by Fig. 10 d and Fig. 10 e. The fact that macroscopic deformation is more accommodated by the α phase, both at low and high levels of deformations, is clearly highlighted by considering the average deformation per phase, see Fig. 11 b. On average, it is now the α phase that is about 30% more deformed than the α'_{dec} phase.

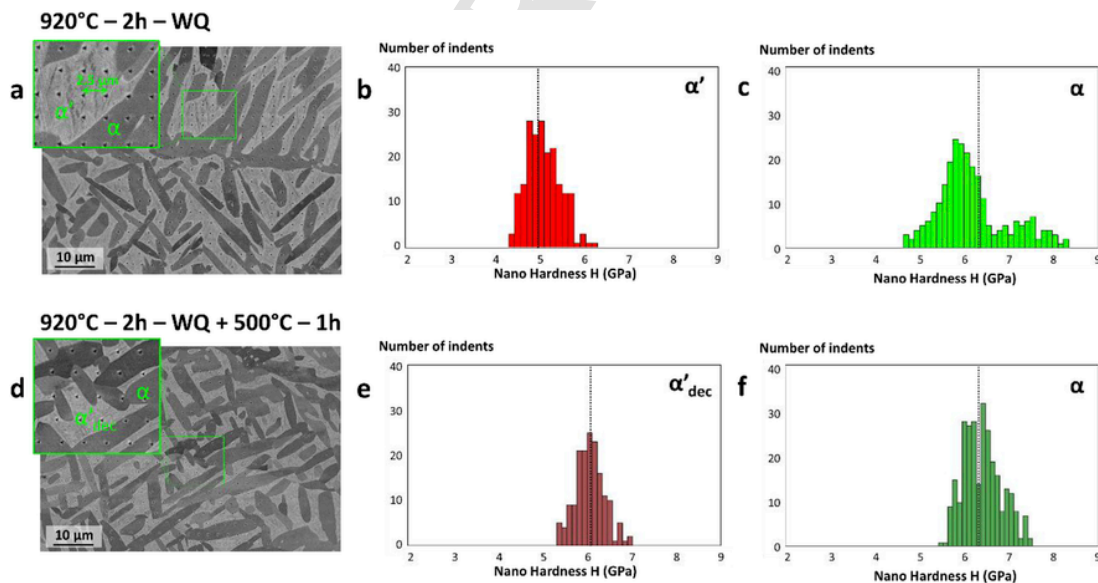


Fig. 8. Nanoindentation measurements For the “920-WQ” specimen: (a) SEM micrograph showing the region of interest with 21×21 indent grid, (b) nano-hardness distribution within the α' -phase (177 indents) and (c) within the α -phase (244 indents). For the “500-1h” specimen: (d) SEM micrograph showing the region of interest with 21×21 indent grid, (e) nano-hardness distribution within the α'_{dec} -phase (163 indents) and (f) within the α -phase (278 indents).

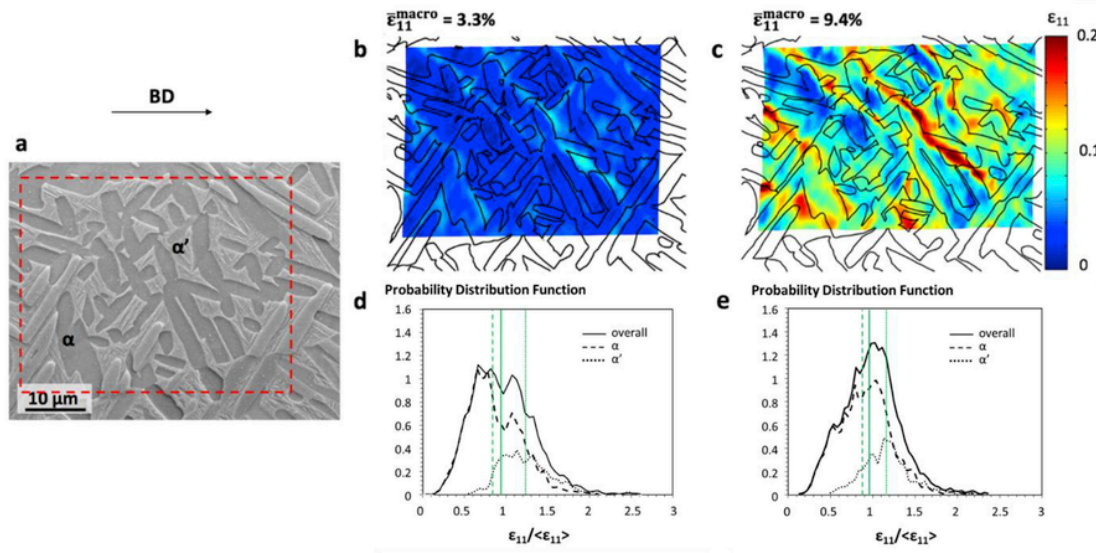


Fig. 9. (a) SEM–SE micrograph of the region of interest for the “920°C-WQ” specimen. Deformation fields obtained by DIC during in-situ tensile tests at two different levels of tensile macroscopic deformation: (b) 3.3% and (c) 9.4%. Note that the tensile macroscopic deformation was estimated by computing the average strain based on the local strains determined over the whole region of interest. Interphase boundaries are highlighted in black. Distribution function of the normalized strain in each phase at (d) 3.3% and (e) 9.4%, in green the mean $\epsilon_{11}/\langle\epsilon_{11}\rangle$ value for each phase. (For interpretation of the references to color in this figure legend, the reader is referred to the Web version of this article.)

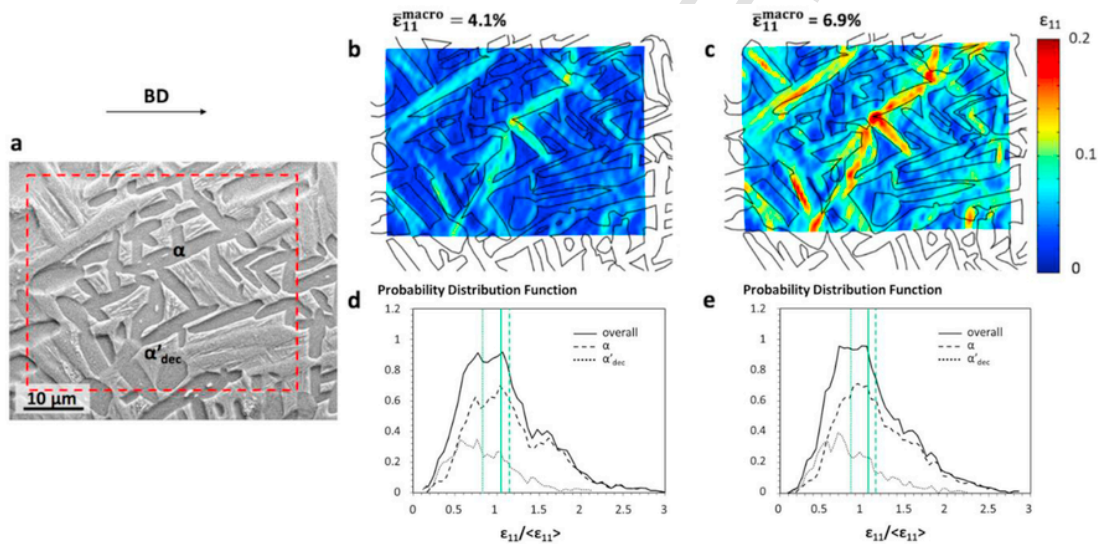


Fig. 10. (a) SEM–SE micrograph of the region of interest for the “500-1h” specimen. Deformation fields obtained by DIC during in-situ tensile tests at two different levels of tensile macroscopic deformation: (b) 4.1% and (c) 6.9%. Note that the tensile macroscopic deformation was estimated by computing the average strain based on the local strains determined over the whole region of interest. Interphase boundaries are highlighted in black. Distribution function of the normalized strain in each phase at (d) 4.1% and (e) 6.9%, in green the mean $\epsilon_{11}/\langle\epsilon_{11}\rangle$ value for each phase. (For interpretation of the references to color in this figure legend, the reader is referred to the Web version of this article.)

It should also be highlighted that, in both specimens, the highest levels of deformation are observed at the interfaces between the two phases and, more particularly, when the soft phase is confined between two lamellae of the harder phase.

4. Discussion

The following discussion will investigate qualitatively the effect of key microstructural features on tensile properties, and describe

more quantitatively, with a simple model, the tensile behavior of each phase and the resulting macroscopic properties. The first part of the discussion will focus on investigating the effect of martensite decomposition on yield strength, whereas the second part will attempt to explain the origin of the unusual work-hardening behavior observed in $\alpha+\alpha'$ Ti–6Al–4V.

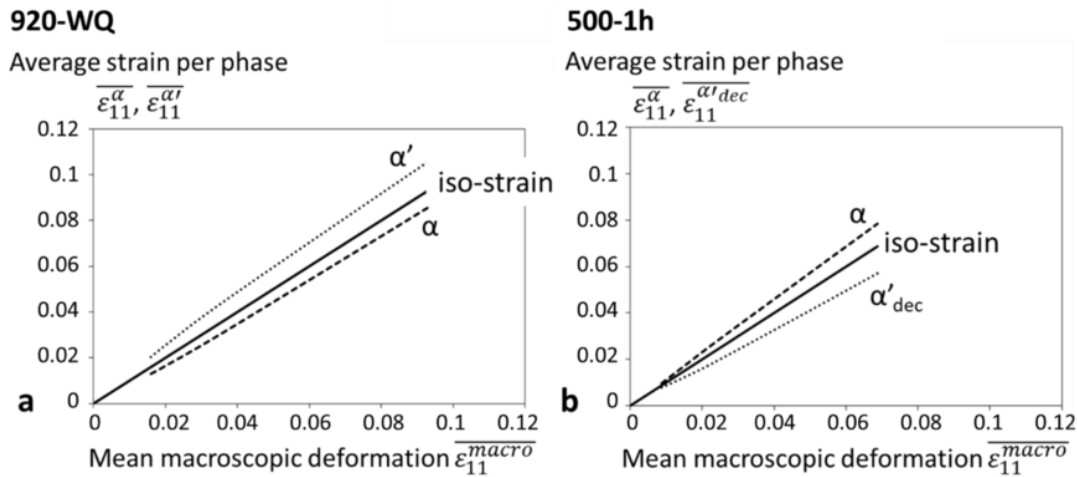


Fig. 11. Average strain per phase as a function of the macroscopic tensile deformation for. (a) The “920-WQ” specimen and (b) “500-1h” specimen.

4.1. Understanding the relationship between microstructure and strength in dual-phase $\alpha+\alpha'$ Ti—6Al—4V and the effect of further annealing

In comparison with the HIP'ed $\alpha+\beta$ material, the dual-phase $\alpha+\alpha'$ microstructure exhibits a very low yield strength. The in-situ tensile tests performed on a “920-WQ” specimen clearly demonstrate that plastic deformation initiates in the martensite, and progressively spreads to adjacent areas. This heterogeneous strain partitioning results in a continuous yielding of the material, starting at low macroscopic stress levels. The mechanical contrast between the relatively soft α' and the harder α phase is also confirmed by the nanoindentation measurements reported in Fig. 8 b and in Fig. 8 c.

As further annealing of the $\alpha+\alpha'$ material is performed, martensite decomposition occurs, which directly impacts the mechanical behavior of the material. After a 1 h annealing at 500 °C, the process of martensite decomposition is clearly incomplete. Indeed, SEM characterization (Fig. 3c) reveals that an acicular microstructure, typical of α' martensite, is still observed in the “500-1h” specimen. Besides, the XRD profile of this specimen exhibits a splitting of the (0002) peak and a broadening of the (10-10) peak which were also observed in the $\alpha+\alpha'$ “920-WQ” material and can be attributed to the presence of α' martensite. However, at the same time, a β peak is observed on the XRD profile of the “500-1h” specimen, and TEM analysis (Fig. 6) clearly highlights the presence of very fine β in the martensitic areas. Although it is possible that β remnants of the fast cooling from the β phase were already present in the “920-WQ” specimens, they were in a too small volume fraction to be detected by XRD. The growth of β grains in the martensitic areas indicates that, after 1 h at 500 °C, the process of martensite decomposition is ongoing. Although they do not form a continuous phase from a microscopic point of view, the decomposing α' lamellae and β particles are here referred to as a “ α'_{dec} ” monotonic phase. The presence of a dispersion of very fine β particles in those α'_{dec} areas induces a substantial hardening of these regions, in a process that is consistent with precipitation hardening. Moreover, from a chemical point of view, alloy element partitioning occurs during annealing, also affecting the yield strength of each phase. In the water quenched $\alpha+\alpha'$ material, as highlighted by EPMA measurements, the primary α is enriched in Al, whereas the α' phase contains a high V-content. The variations in the lattice parameter of the β phase generated during decomposition can be related to changes

in the V content of the β phase. As shown in Fig. 4 b, the low lattice parameter of the samples treated at 500 °C for 1 h indicates that the β phase in these specimens contained a high amount of V, since V has lower atomic radius (0.132 nm) than Ti (0.146 nm) [33]. The temperature and duration of the treatment dictates the amount of β phase that is generated in the process of martensite decomposition and the V content in the β phase. It can be hypothesized that the low amounts of β phases generated at the early stages of decomposition contain a high amount of V, which decreases as the β grains coarsen and the fraction of β increases. Similarly, Xu et al. observed that finer β laths exhibit much higher V content than coarser ones [34]. The process of martensite decomposition during annealing is thus diffusion-controlled, with Al progressively segregating into the α' martensite lamellae, while V is being rejected to the small β grains surrounding these lamellae. This local partitioning taking place within the α'_{dec} areas results in V-enriched precipitates and Al-enriched lamellae. Al being a potent solid solution strengthener [35,36], the increase in Al content induces a local hardening of the lamellae. In-situ tensile tests show that the α'_{dec} phase becomes harder than the α phase in the “500-1h” material, although the α phase was initially harder in the “920-WQ” material. The combination of both *solution-strengthening* by local Al-enrichment and *precipitation hardening* can account for the 1 GPa increase in nano-hardness of the α'_{dec} phase. It also directly impacts the macroscopic tensile properties of the material, which sees its yield strength increase by more than 250 MPa.

In specimens treated at a higher temperature, the process of martensite decomposition is more advanced. SEM analysis reveals that the acicular microstructure initially present in the dual-phase microstructure is no longer observed after annealing at 700 °C, even for a duration as short as 5 min. Besides, no splitting or broadening of the α peaks is visible in the XRD profiles of these specimens, whereas a stronger β peak is present. These observations suggest that complete decomposition of the martensite occurs at 700 °C, even when short annealing times are considered. A 1 h annealing time at 700 °C results in a further coarsening of the secondary α lamellae and β rods resulting from martensite decomposition. An $\alpha+\beta$ microstructure with a bimodal grain size distribution is thus obtained. This microstructure contains about 50% of primary α grains inherited from the HIP operation. These α grains are relatively coarse (3–4 μm) and mostly lamellar – although some are nearly globular. The rest of the microstructure consists of fine secondary α lamellae (~250 nm) delineated by thin β rods, which are transformation products of the

martensite decomposition. In this $\alpha+\beta$ microstructure, the small size of the secondary α lamellae induces a *grain size strengthening* (significant increase of the number of interfaces), resulting in a higher yield strength than the one obtained in the coarse unimodal $\alpha+\beta$ microstructure of the as-HIP'ed material.

This microstructure can be related to “duplex” or “bimodal” microstructures, which are valued for their good balance between strength and ductility and their superior fatigue strength [32]. In wrought Ti-6Al-4V, they are obtained by a multistep process that includes hot working and recrystallization in the $\alpha+\beta$ phase field [24]. They consist of a mixture of coarse equiaxed primary α and fine lamellar secondary α resulting from the cooling of the β phase. It should be highlighted here that the two-step processing route consisting in a quench from the $\alpha+\beta$ phase field followed by a short annealing at 700 °C allows the material to transition from a fully lamellar to a more balanced bimodal microstructure without any hot working being involved. This would be a major industrial asset. A finer control of this microstructure could be achieved: the phase fraction and size of the primary α directly depend on the temperature and duration of the sub-transus treatment [25], respectively, whereas the thickness of the secondary α lamellae is related to the temperature and duration of the annealing treatment used to achieve martensite decomposition.

4.2. Modeling the work-hardening behavior of multiphase microstructures

The 50% α + 50% α' material obtained after a 2 h treatment at 920 °C followed by water quenching exhibits a remarkable work-hardening, which induces a desirable increase in both ultimate tensile strength and uniform strain (Table 2). As reported for other heterogeneous materials, such as dual-phase (DP) steels [37–39] and ferrite-pearlite steels [40], the origin of this work-hardening can be attributed to the presence of a mechanical contrast between the two phases. Indeed, when deforming such a composite microstructure, the softest phase is the first to deform plastically, while the hardest remain elastic. After a certain amount of deformation, the initial apparent work-hardening is enhanced when compared to the work-hardening of the softest phase. The difference in behavior between soft and hard components of the microstructure will sustain this effect as the soft phases will deform more than hard phases. A dual-phase microstructure thus naturally induces an additional work-hardening when compared to the individual constituting phases [41].

Here, both the nanoindentation measurements (Fig. 8 b and Fig. 8c) and the in-situ tensile tests (Figs. 9 and 11a) show that the α' martensite appears to be softer than the α phase. The mechanical contrast between α' martensite and α is in this case not as high and in the reverse order as in DP steels [42], composed of soft ferrite and hard martensite (relatively high carbon content), but stands a comparison with the mechanical contrast observed between ferrite and pearlite [43].

Annealing of the dual-phase $\alpha+\alpha'$ material has a substantial impact on work-hardening. Fig. 7 c clearly highlights that, in the continuous process of martensite decomposition, the work-hardening behavior becomes progressively closer to that of the as-HIP'ed $\alpha+\beta$ typical microstructure. In particular, the fully decomposed specimens exhibit a relatively small work-hardening rate at low strains but a stabilization or increase of the work-hardening rate at higher strains. In other words, although the specimens annealed at 700 °C differ from the as-HIP'ed specimen in terms of yield strength, they exhibit a very similar work-hardening behavior.

In order to reach a more quantitative understanding of the tensile behavior of the dual-phase $\alpha+\alpha'$ microstructure, an analytical model

based on the behavior of each phase was developed. Two distinct microstructures were considered: the $\alpha+\alpha'$ microstructure obtained by a 2 h treatment at 920 °C followed by water quenching, and the $\alpha+\alpha'_{dec}$ microstructure resulting from a further 1 h annealing at 500 °C.

The constitutive behavior of each phase was implemented by considering that dislocation glide is impeded by two sets of obstacles, namely forest dislocations and strong precipitates. Because these obstacles act on similar scales, a linear superposition of their contributions cannot be applied [44]. Indeed, in this case, according to Kocks et al. [44], the obstacle densities can be added so that the following superposition law is obtained:

$$\sigma = \sqrt{\sigma_d^2 + \sigma_p^2} \quad (1)$$

where σ_d corresponds to the glide resistance caused by dislocations, and σ_p to that associated with precipitates.

σ_p is a constant, which equals 0 if no precipitates are present in the phase.

σ_d follows the classical Taylor evolution:

$$\sigma_d = \sigma_0 + M\alpha\mu b\sqrt{\rho} \quad (2)$$

where M is the Taylor factor, α is a constant, μ the shear modulus, b the magnitude of the Burgers vector, ρ the dislocation density and σ_0 the lattice strength [45].

The evolution of the dislocation density ρ with strain is given by:

$$\frac{d\rho}{d\varepsilon} = M(k_1\sqrt{\rho} - k_2\rho) \quad (3)$$

where $k_1\sqrt{\rho}$ is a storage term due to dislocation-dislocation pinning and $k_2\rho$ is an annihilation contribution due to dynamic recovery [45]. The values of these terms are reported in Table 3.

In order to describe the load transfers and deformation partitioning between the two phases, different homogenization schemes can be applied, the simplest ones being the iso-strain and the iso-stress assumptions. However, these approaches respectively provide the upper and lower bounds of the problem rather than the realistic solution. Here, the iso-work (IsoW) assumption, initially proposed by Bouaziz et al. [46], was considered. This approach relies on the assumption that the dissipation of the plastic work is equal in each phase:

Table 3
Description, symbol, magnitude and unit of the different parameters of the model.

Parameter	Symbol	Magnitude	Unit
Volume fraction of martensite	V_m	0.5	–
Taylor factor	M	5	–
Taylor constant	α	1	–
Shear modulus	μ	44	GPa
Burgers vector magnitude	b	2.95E-10	m
Initial dislocation density	ρ_0	1.00E+12	m ⁻²
Yield strength (α')	$\sigma_0^{\alpha'}$	728	MPa
Yield strength (α)	σ_0^{α}	1018	MPa
Yield strength (α'_{dec})	$\sigma_0^{\alpha'_{dec}}$	1130	MPa
σ_p	σ_p	960	MPa
Storage constant (α')	$k_1^{\alpha'}$	3.8E+07	m ⁻¹
Storage constant (α)	k_1^{α}	4.0E+07	m ⁻¹
Dynamic recovery constant (α')	$k_2^{\alpha'}$	15.0	–
Dynamic recovery constant (α)	k_2^{α}	12.3	–
Young's modulus	$E^{\alpha'} = E^{\alpha}$	114	GPa

$$\sigma_1.d\epsilon_1^p = \sigma_2.d\epsilon_2^p$$

where ϵ^p stands for the plastic strain.

As elastic strains can be neglected, the total strains in each phase were considered in the calculation, so that:

$$\sigma_1.d\epsilon_1 = \sigma_2.d\epsilon_2$$

Sub-scripts 1 and 2 refer to the constituting phases of the heterogeneous microstructure. The validity of this iso-work assumption has been extensively studied by Montheillet et al. [47]. These authors have shown that if the stress contrast between constituting phases is limited and their fractions are similar, this approach leads to a macroscopic behavior which is similar to common self-consistent schemes, with an undeniable calculation efficiency. Beyond its simplicity, the main advantage of the iso-work assumption is also the absence of calibration parameters. The iso-work model has been successfully applied to heterogeneous steel microstructures, such as Ferrite-Martensite Dual-Phase [40] or Ferrite-Pearlite steels [39].

In order to further refine the model, the following assumptions, derived from previously detailed experimental observations were made for the “920-WQ” material:

- (i) The soft α' martensite has a yield strength lower than 825 MPa (i.e. the yield strength of the dual-phase material).
- (ii) Based on the nanoindentation measurements, indicating a hardness of 6.28 ± 0.65 GPa for the α phase and of 4.97 ± 0.3 GPa for the α' phase (i.e. a ratio between the two equal to 1.26), the ratio between the ultimate tensile strength of the α phase and that of the α' phase was considered equal to 1.26.
- (iii) The difference between the average deformation in one phase and that in the other, for a given average macroscopic deformation, can be obtained from the in-situ measurements reported in Fig. 11. Note that the average macroscopic deformation was computed from all the local strain measurements within the region of interest. It was considered that the difference in mean deformation between α' -martensite and α at a mean macroscopic deformation of 0.09 was equal to 0.02 for the “920-WQ” material.

The Young's modulus E was chosen as being equal to 114 GPa in both phases.

The values for k_1 and k_2 for each phase, reported in Table 3, were obtained by minimizing the difference between the experimental tensile curve and the modeled one, using a least squares approach.

Fig. 12 a compares the model's predictions with the experimental true stress-true strain curves. The tensile behavior of each phase is also reported. Although the simple model developed here does not allow the smooth elasto-plastic transition to be precisely predicted, a good agreement with the experimental data is achieved.

The same model was implemented for the “500-1h” material. Apart from the yield strength of the α'_{dec} phase and the value of σ_p ($\sigma_p = 960$ MPa), the other parameters, namely k_1 and k_2 , were kept constant. In addition, the following assumptions were made:

- (i) The precipitation-hardened and solution-strengthened α'_{dec} phase in the “500-1h” specimen has a yield strength higher than 1088 MPa (i.e. the yield strength measured experimentally for the “500-1h” material).
- (ii) Based on the nanoindentation measurements, indicating similar hardness values for the α and α'_{dec} phases in the “500-1h” mater-

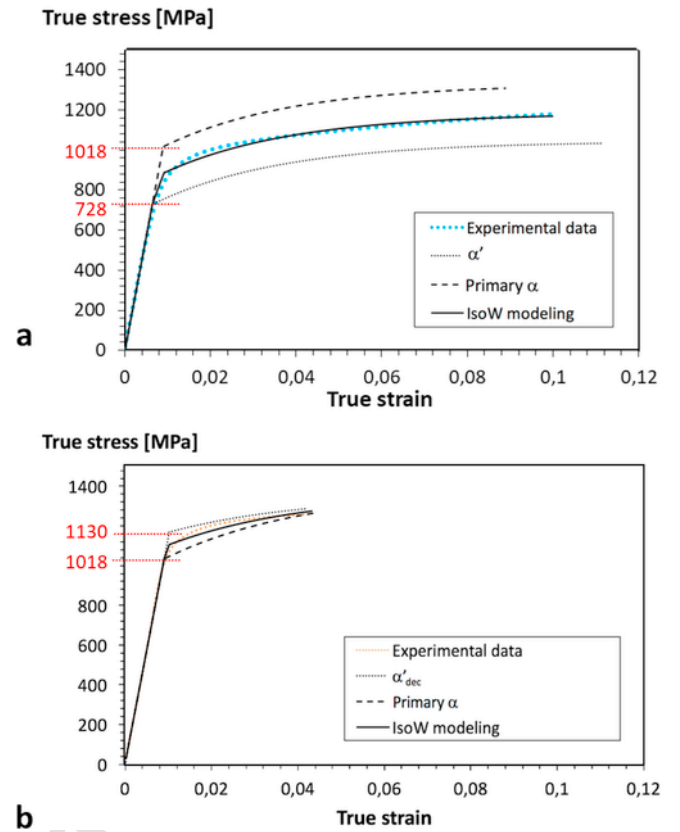


Fig. 12. Modeling of the stress-strain curves for the “920-WQ” material (a), and for the “500-1h” material (b). The modeling of the dual-phase material from the individual behavior of each phase is based on the IsoW assumption.

ial, the ultimate tensile strength of the α phase was considered equal to that of the α'_{dec} phase.

In order to obtain an adequate fitting of the model with the experimental results, a yield strength of 1130 MPa was considered for the precipitation-hardened and solution-strengthened α'_{dec} phase. This high yield strength can be easily explained by the diffusion of V from the decomposing martensite, concomitant formation of V-rich β precipitates and corresponding Al enrichment of the decomposing martensite lamellae. The resulting modeling is reported in Fig. 12 b. Again, a good agreement with the experimental data is achieved.

In the “500-1h” material, the lower work-hardening in the α'_{dec} phase can be attributed to the presence of precipitates. Indeed, if we derive equation (1), we obtain:

$$\frac{d\sigma}{d\epsilon} = \frac{\sigma_d}{\sqrt{\sigma_d^2 + \sigma_p^2}} \frac{d\sigma_d}{d\epsilon} \quad (4)$$

where $\frac{d\sigma}{d\epsilon} = \theta$ is the work-hardening rate.

However, if no precipitates are present, we have $\sigma_p = 0$ and equation (4) becomes:

$$\frac{d\sigma}{d\epsilon} = \frac{d\sigma_d}{d\epsilon} > \frac{\sigma_d}{\sqrt{\sigma_d^2 + \sigma_p^2}} \frac{d\sigma_d}{d\epsilon} \quad (5)$$

In other words, the existence of small shearable precipitates tends to decrease the work-hardening rate. In addition, the lower mechanical contrast between the α and the α'_{dec} phases further decreases the work-hardening of the “500-1h” material, compared to the $\alpha+\alpha'$ microstructure.

Although based on a simple “iso-work” approach, the model developed here clearly demonstrates how the mechanical contrast between two phases induces work-hardening. It also highlights the mechanisms leading to a decrease in work-hardening when the martensite decomposes. However, the α' and α'_{dec} phases should be considered as non-homogeneous media in order to be able to more properly capture size effects and the role of interfaces. Consequently, from a modeling perspective, future investigations should include more local approaches where, for example, a representative element of the microstructure is discretized and the local strain and stress fields can be computed and compared to experimental data. From an experimental perspective, Bauschinger tests would allow to quantitatively determine the kinematic contribution to work-hardening brought about by the mechanical contrast between the phases.

5. Conclusions

The high work-hardening behavior observed in $\alpha+\alpha'$ Ti–6Al–4V results from a difference in yield strength between the soft α' martensite and the harder α phase. This mechanical contrast was demonstrated by in-situ tensile tests coupled with DIC measurements of strain partitioning between the phases and confirmed by nanoindentation measurements.

Annealing the material at 500 °C leads to a major shift in the mechanical behavior of the dual-phase material: the α'_{dec} phase, strengthened by a dispersion of fine β precipitates, becomes harder, and plastic deformation is initiated in the α phase. Precipitation hardening of the α'_{dec} phase also results in a decrease in work-hardening. This is highlighted by the model developed here. Indeed, although the decomposing martensite is stronger than the α phase, its work-hardening rate is considerably lower. At higher annealing temperatures, the martensite fully decomposes to fine secondary α lamellae and β rods. The resulting microstructure exhibits a low work-hardening, as conventionally reported in $\alpha+\beta$ Ti–6Al–4V.

The thermal treatments investigated in this paper enable to generate a large variety of microstructures. A broad range of mechanical properties – strength, ductility, work-hardening – can be achieved by exploring new processing routes. Microstructural engineering through the development of innovative thermal treatments is particularly interesting when considering near-net shape titanium parts which cannot undergo further hot working, as is the case for additively manufactured parts.

Acknowledgements

The authors are grateful to the F.R.I.A. - F.N.R.S. For financing this research. The authors wish to acknowledge the help of Ing. Marc Sinnaeve from the IMAP department (Université Catholique de Louvain) and Dr. Loïc Malet from the 4MAT department (Université Libre de Bruxelles). This work was partly performed within the framework of the Center of Excellence of Multifunctional Architected Materials “CEMAM” noAN-10-LABX-44-01 funded by the “Investments for the Future Program”.

References

- [1] M. Peters, J. Kumpfert, C.H. Ward, C. Leyens, Titanium alloys for aerospace applications, *Adv. Eng. Mater.* 5 (2003) 419–427.
- [2] K. Wang, The use of titanium for medical applications in the USA, *Mater. Sci. Eng.* 213 (1996) 134–137.
- [3] M. Niinomi, Mechanical properties of biomedical titanium alloys, *Mater. Sci. Eng.* 243 (1998) 231–236.
- [4] A.R. Machado, J. Wallbank, Machining of titanium and its alloys – a review, *Proc. Inst. Mech. Eng. Part B J. Eng. Manuf.* 204 (1990) 53–60.
- [5] B. Dutta, F.H. Froes, The Additive Manufacturing (AM) of titanium alloys, *Met. Powder Rep.* 72 (2017) 96–106.
- [6] C. Qiu, N.J.E. Adkins, M.M. Attallah, Microstructure and tensile properties of selectively laser-melted and of HIPed laser-melted Ti–6Al–4V, *Mater. Sci. Eng.* 578 (2013) 230–239.
- [7] D. Greitemeier, C. Dalle Donne, F. Syassen, J. Eufinger, T. Melz, Effect of surface roughness on fatigue performance of additive manufactured Ti-6Al-4V, *Mater. Sci. Technol.* 32 (2016) 629–634.
- [8] Y.Y. Sun, S. Gulizia, C.H. Oh, D. Fraser, Y.F. Leary, Y.F. Yang, M. Qian, The influence of as-built surface conditions on mechanical properties of Ti-6Al-4V additively manufactured by selective electron beam melting, *J. Occup. Med.* 68 (2016) 791–798.
- [9] S. Tammas-Williams, P.J. Withers, I. Todd, P.B. Prangnell, The effectiveness of hot isostatic pressing for closing porosity in titanium parts manufactured by selective electron beam melting, *Metall. Mater. Trans.* 47 (2016) 1939–1946.
- [10] S.M. Gaytan, L.E. Murr, E. Medina, M.I. Lopez, R.B. Wickler, Advanced metal powder based manufacturing of complex components by electron beam melting, *Mater. Technol.* 24 (2013) 180–190.
- [11] P. Mercelis, J.P. Kruth, Residual stresses in selective laser sintering and selective laser melting, *Rapid Prototyp. J.* 12 (2006) 254–295.
- [12] T. Persenot, G. Martin, R. Dendievel, J.-Y. Buffière, E. Maire, Enhancing the tensile properties of EBM as-built thin parts: effect of HIP and chemical etching, *Mater. Charact. Press* (2018).
- [13] C. de Formanoir, M. Suard, R. Dendievel, G. Martin, S. Godet, Improving the mechanical efficiency of electron beam melted titanium lattice structures by chemical etching, *Addit. Manuf.* 11 (2016) 71–76.
- [14] P. Lhuissier, C. de Formanoir, G. Martin, R. Dendievel, S. Godet, Geometrical control of lattice structures produced by EBM through chemical etching: investigations at the scale of individual struts, *Mater. Des.* 110 (2016) 485–493.
- [15] S.L. Lu, H.P. Tang, Y.P. Ning, N. Liu, D.H. StJohn, M. Qian, Microstructure and mechanical properties of long Ti-6Al-4V rods additively manufactured by selective electron beam melting out of a deep powder bed and the effect of subsequent hot isostatic pressing, *Metall. Mater. Trans.* 46 (2015) 3824–3834.
- [16] T. Vilaro, C. Colin, J.D. Bartout, As-Fabricated and heat-treated microstructures of the Ti-6Al-4V alloy processed by selective laser melting, *Metall. Mater. Trans.* 42 (2011) 3190–3199.
- [17] X. Zhao, S. Li, M. Zhang, Y. Liu, T.B. Sercombe, S. Wang, Y. Hao, R. Yang, L.E. Murr, Comparison of the microstructures and mechanical properties of Ti–6Al–4V fabricated by selective laser melting and electron beam melting, *Mater. Des.* 95 (2016) 21–31.
- [18] L. Facchini, E. Magalini, P. Robotti, A. Molinari, S. Höges, K. Wissenbach, Ductility of a Ti-6Al-4V alloy produced by selective laser melting of prealloyed powders, *Rapid Prototyp. J.* 16 (2010) 450–459.
- [19] N. Hrabe, T. Gnaüpel-Herold, T. Quinn, Fatigue properties of a titanium alloy (Ti–6Al–4V) fabricated via electron beam melting (EBM): effects of internal defects and residual stress, *Int. J. Fatig.* 94 (2017) 202–210.
- [20] B. Vrancken, L. Thijs, J.P. Kruth, J. Van Humbeeck, Heat treatment of Ti6Al4V produced by selective laser melting: microstructure and mechanical properties, *J. Alloy. Comp.* 541 (2012) 177–185.
- [21] S. Cao, R. Chu, R. Zhou, K. Yang, Q. Jia, C.V.S. Lim, A. Huang, X. Wu, Role of martensite decomposition in tensile properties of selective laser melted Ti-6Al-4V, *J. Alloy. Comp.* (2018).
- [22] S.S. Al-Bermani, M.L. Blackmore, W. Zhang, I. Todd, The origin of microstructural diversity, texture, and mechanical properties in electron beam melted Ti-6Al-4V, *Metall. Mater. Trans.* 41 (2010) 3422–3434.
- [23] X. Shui, K. Yamanaka, M. Mori, Y. Nagata, K. Kurita, A. Chiba, Effects of post-processing on cyclic fatigue response of a titanium alloy additively manufactured by electron beam melting, *Mater. Sci. Eng.* 680 (2017) 239–248.
- [24] G. Lütjering, Influence of processing on microstructure and mechanical properties of $(\alpha+\beta)$ titanium alloys, *Mater. Sci. Eng.* 243 (1998) 32–45.
- [25] C. de Formanoir, A. Brulard, S. Vivès, G. Martin, F. Prima, S. Michotte, E. Rivière, A. Dolimont, S. Godet, A strategy to improve the work-hardening behavior of Ti–6Al–4V parts produced by additive manufacturing, *Mater. Res. Lett.* 5 (2016) 201–208.

- [26] C. de Formanoir, S. Michotte, O. Rigo, L. Germain, S. Godet, Electron beam melted Ti-6Al-4V: microstructure, texture and mechanical behavior of the as-built and heat-treated material, *Mater. Sci. Eng.* 652 (2016) 105–119.
- [27] L. Allais, M. Bornert, T. Bretheau, D. Caldemaison, Experimental Characterization of the local strain field in a heterogeneous elastoplastic material, *Acta Metall. Mater.* 42 (1994) 3865–3880.
- [28] E. Héripré, M. Dextet, J. Crépin, L. Gélébart, A. Roos, M. Bornert, D. Caldemaison, Coupling between experimental measurements and polycrystal finite element calculations for micromechanical study of metallic materials, *Int. J. Plast.* 23 (2007) 1512–1539.
- [29] G. Martin, D. Caldemaison, M. Bornert, C. Pinna, Y. Bréchet, M. Véron, J.D. Mithieux, T. Pardoen, Characterization of the high temperature strain partitioning in duplex steels, *Exp. Mech.* 53 (2013) 205–215.
- [30] G. Martin, S.K. Yerra, Y. Bréchet, M. Véron, J.D. Mithieux, B. Chéhab, L. Delannay, T. Pardoen, A macro- and micromechanics investigation of hot cracking in duplex steels, *Acta Mater.* 60 (2012) 4646–4660.
- [31] A. Lechartier, G. Martin, S. Comby, S. Roussel-Dherbey, A. Deschamps, M. Mantel, N. Meyer, M. Verdier, M. Véron, Influence of the martensitic transformation on the microscale plastic strain heterogeneities in a duplex stainless steel, *Metall. Mater. Trans.* 48 (2017) 20–25.
- [32] A.K. Sachdev, Effect of retained austenite on the yielding and deformation behavior of a dual phase steel, *Acta Metall.* 31 (1983) 2037–2042.
- [33] E. Sallica-Leva, R. Caram, A.L. Jardini, J.B. Fogagnolo, Ductility improvement due to martensite α' decomposition in porous Ti-6Al-4V parts produced by selective laser melting for orthopedic implants, *J. Mech. Behav. Biomed. Mater.* 54 (2016) 149–158.
- [34] W. Xu, M. Brandt, S. Sun, J. Elambasseril, Q. Liu, K. Latham, K. Xia, M. Qian, Additive manufacturing of strong and ductile Ti-6Al-4V by selective laser melting via in situ martensite decomposition, *Acta Mater.* 85 (2015) 74–84.
- [35] R. Boyer, G. Welsch, *Materials Properties Handbook: Titanium Alloys*, ASM International, 1994.
- [36] B.J. Hayes, B.W. Martin, B. Welk, S.J. Kuhr, T.K. Ales, D.A. Brice, I. Ghamarian, A.H. Baker, C.V. Haden, D.G. Harlow, H.L. Fraser, P.C. Collins, Predicting tensile properties of Ti-6Al-4V produced via directed energy deposition, *Acta Mater.* 133 (2017) 120–133.
- [37] L. Zhonghua, G. Haicheng, Bauschinger effect and residual phase stresses in two ductile-phase steels: Part I. The influence of phase stresses on the Bauschinger effect, *Metall. Trans. A.* 21 (1990) 717–724.
- [38] L. Zhonghua, G. Haicheng, Bauschinger effect and residual phase stresses in two ductile-phase steels: Part II. The effect of microstructure and mechanical properties of the constituent phases on Bauschinger effect and residual phase stresses, *Metall. Trans. A.* 21 (1990) 725–732.
- [39] S. Allain, O. Bouaziz, I. Pushkareva, C.P. Scott, Towards the microstructure design of DP steels: a generic size-sensitive mean-field mechanical model, *Mater. Sci. Eng.* 637 (2015) 222–234.
- [40] S. Allain, O. Bouaziz, Microstructure based modeling for the mechanical behavior of ferrite-pearlite steels suitable to capture isotropic and kinematic hardening, *Mater. Sci. Eng.* 496 (2008) 329–336.
- [41] R.J. Asaro, Elastic-plastic memory and kinematic-type hardening, *Acta Metall.* 23 (1975) 1255–1265.
- [42] C.C. Tasan, M. Diehl, D. Yan, C. Zambaldi, P. Shanthraj, F. Roters, D. Raabe, Integrated experimental-simulation analysis of stress and strain partitioning in multiphase alloys, *Acta Mater.* 81 (2014) 386–400.
- [43] C.C. Tasan, J.P.M. Hoefnagels, M.G.D. Geers, Microstructural banding effects clarified through micrographic digital image correlation, *Scripta Mater.* 62 (2010) 835–838.
- [44] U.F. Kocks, A.S. Argon, M.F. Ashby, *Thermodynamics and Kinetics of Slip*, in: Bruce Chalmers, J.W. Christian, T.B. Massalski (Eds.), Pergamon Press, Oxford, UK, 1975.
- [45] M. Delincé, Y. Bréchet, J.D. Embury, M.G.D. Geers, P.J. Jacques, T. Pardoen, Structure-property optimization of ultrafine-grained dual-phase steels using a microstructure-based strain hardening model, *Acta Mater.* 55 (2007) 2337–2350.
- [46] O. Bouaziz, P. Büessler, Iso-work increment assumption for heterogeneous material behavior modelling, *Adv. Eng. Mater.* 6 (2004) 79–83.
- [47] F. Montheillet, G. Damamme, Simple flow rules for modeling the behaviour of inhomogeneous viscoplastic materials, *Adv. Eng. Mater.* 7 (2005) 852–858.